Supplementary Information (SI) for Journal of Materials Chemistry A.

Supporting Information

Dual-functional S-scheme Ti_3C_2/MoS_2-$ZnIn_2S_4$ heterojunction for accelerate photocatalytic H_2 evolution and efficient solar evaporators

Xin Xiong[#,1], *Longji Gui*[#,1], *Li Yang*[2], *Jintao Li*[1], *Songsong Xu*[1], *Fang Yu*[*,2], *Tao Mei*[1], *Jinwen Qian*[*,1], *Xianbao Wang*[*,1]

E-mail: FangYu@ycit.edu.cn (Dr. Fang Yu) qianjingwen@hubu.edu.cn (Dr. Jingwen Qian) wxb@hubu.edu.cn (Prof. Dr. Xianbao Wang)

S1. Materials and methods

1.1 Materials

$InCl_3 \cdot 4H_2O$ (≥99%), thioacetamide (TAA, ≥99%). glycerol (≥99%) were purchased from Shanghai Macklin Biochemical Co. Ltd. Thioacetamide (C_2H_5NS), ammonium molybdate ($(NH_4)_6Mo_7O_{24} \cdot 4H_2O$), citric acid, thioacetamide, Ltd (China)., Lignin and sodium alginate (SA) were supplied from Macklin Biochemical Co., Ltd (Shanghai, China). Ti_3AlC_2 purchased from Shandong R&EN New Materials Co.

1.2 Synthesis of two-dimensional organ-shaped Ti_3C_2

1.0 g of Ti_3AlC_2 powder was slowly added to 30 mL of HF solution (40 wt%) and stirred in an ice-water bath at room temperature for 72 h. The suspension was separated by centrifugation at 10000 r/min to remove the supernatant, and then washed repeatedly with deionized water and ethanol until the suspension pH≥6. The treated suspension was dried under vacuum at 60°C for 2 hours to obtain organ-shaped Ti_3C_2.[1]

1.3 Synthesis of composite photothermal material Ti_3C_2/MoS_2

Typically, 0.13 g of organ-shaped Ti_3C_2 was fully dissolved in 40 ml of water by ultrasonication for 10 min. And 0.35 g $(NH_4)_6Mo_7O_{24} \cdot 4H_2O$ and 0.7 g C_2H_5NS and

0.09 g citric acid were added into a flat-bottomed beaker with a 100 mL capacity under constantly strong magnetic stirring for 30 min. Then, the suspension was put into the PTFE lining with a 50 mL capacity and kept at 200 °C for 24 h. The obtained product was washed by deionized water and ethanol about 3 times respectively, then dried in vacuum at 60 °C until the powder was dried completely.[2]

1.4 Synthesis of ternary composite $ZnIn_2S_4/Ti_3C_2/MoS_2$ photothermal-photocatalyst

0.1 g Ti_3C_2/MoS_2, 80 ml hydrochloric acid solution at pH=2.5 and 20 ml glycerol were thoroughly mixed into a 150 ml round bottom flask and sonicate for 20 minutes and then 0.272 g $ZnCl_2\cdot 2H_2O$ and 0.586 g $InCl_3\cdot 4H_2O$ and 0.3 g thioacetamide were added sequentially. Finally, the reaction in oil bath at 80 °C for 2h. The obtained product was washed by deionized water about 3 times respectively, then dried in vacuum at 60 °C until the powder was dried completely.[3]

1.5 Synthesis of the Natural Silk Nano-fifibrils (SNFs)

Briefly, 20 g of domestic silkworm cocoon flakes were degassed in 1 L of sodium carbonate solution (0.1 wt%) at 100°C for 30 min, rinsed thoroughly and dried in an oven for 12 h. The extracted silk fibrin fibers were immersed in a ternary solvent of calcium chloride, CH_3CH_2OH and H_2O (molar ratio: 1:2:8) with a 1:250 g mL^{-1} bath ratio for 6 h. Subsequently, the silk fibers were removed from the ternary solvent (the ternary solvent could be preserved and recovered) and rinsed thoroughly with deionized water. Subsequently, the silk fibers were removed from the ternary solvent (the ternary solvent could be saved and recovered) and rinsed thoroughly with deionized water. The pretreated silk fibrin fibers were cut into ~1 cm lengths and well dispersed in deionized water.[3]

1.6 Synthesis of ternary composite $ZnIn_2S_4/Ti_3C_2/MoS_2$ natural silk nano-fibril aerogels ($ZnIn_2S_4/Ti_3C_2/MoS_2$ SNFAs)

The dried SNFs was redispersed with deionized water by a high-speed blender (500 r min^{-1}) to disperse SNFs and obtain a 2~8 (mg mL^{-1}) SNF suspension. Poly (vinyl alcohol) (PVA, 1750 Da, Sinopharm, Shanghai, China) was dissolved in deionized water at 90 °C to prepare a PVA solution. 20g SNFs and 0.1g $ZnIn_2S_4/Ti_3C_2/MoS_2$ were mixed with the 2.0g PVA solution and stirred to form a homogeneous blend solution. The mixed solution was quickly poured into a metal dish and frozen at -20°C for 24 h. After freeze-drying for 48 h, SNFAs were obtained.

1.7 Material Characterization

The phase structure of the samples was analyzed using x-ray diffraction (XRD, Bruker D8 phaser) at 40 kV and 200 mA of copper radiation. The samples were characterized by field emission scanning electron microscopy (FESEM, JSM7100F, Japan) and high energy x-ray spectrometer (EDX) to analyze the elemental distribution of the samples. The photonic transmittance (T) and reflflectance (R) were obtained in the range of 250−2500 nm by ultraviolet−visible−near-infrared spectrophotometer (Shimadu UV−vis−NIR UV-3600 double beam spectrophotometer) with an integrating sphere. The light absorbance (A) was calculated by $A = 1-T-R$. Raman spectra were acquired using a Raman microscope with a 532 nm excitation laser (LabRAMHR800 UV, France). The photoluminescence (PL) spectra and time-resolved photoluminescence (TRPL) spectra of the samples were collected on a Perkin Elmer LS55 spectrophotometer with an excitation laser of 375 nm. The chemical states of the elements of the synthesized photocatalysts were investigated by X-ray photoelectron spectroscopy (PHOIBOS150, Germany). The elemental composition was measured by X-ray photoelectron spectroscopy (XPS) (THERMOFISHERSICENTIFIC Escalab 250Xi) with a monochromatic Mg Ka X-ray source. The mechanical properties of SNFAs materials were tested by the high and low temperature material testing machine (INSRON 68TM-10, USA). The contact angle images of clean films were recorded by using a JY-82 equipment at room temperature.

1.8 Solar Evaporating Setup

Solar-driven evaporation experiments were carried out by employing a solar simulator (PLS-FX300HU) device that can yield multiple solar intensities up to 10 kW m^{-2} (10 suns). An optical fifilter was applied to obtain a standard AM 1.5G spectrum. SNFAs with a thickness of 1.5 cm were floated on bulk water and simulated seawater for desalination tests in a glass container with the sample surface was set to a solar intensity beam point. The mass change of water in the container were recorded by an electronic analytical balance (Mettler-Toledo, ME204) with a resolution of 0.001 g. The evaporation rates determined in the experiments were all measured after 30 minutes of stabilization under one solar illumination. The surface temperature of the NSA was monitored by infrared thermography (FLIR E4 Pro, USA), and two thermocouples were positioned on the surface and bottom of the sample. The ion concentrations of seawater and condensate were estimated by an inductively coupled plasma-optical emission spectrometer (ICP-OES, EP Optimal 8000). All tests were executed at ambient temperature (24 ~26 °C) and humidity of 50 ~55%. The outdoor experiments were conducted during the daytime (8:00-18:00) on the rooftop of Hubei University. The mass change of SNFAs was registered with an electronic analytical balance (error 0.01 g) under natural light. Outdoor solar radiation density and surface temperature were monitored by a handheld optical instrument model and thermocouples, respectively.

1.9 Photocatalytic H_2 evolution experiment

The photocatalytic H_2 generation were performed using an automatic on-line catalytic system for the evolution of photocatalytic activity (BEIJING CHINA EDUCATION AU-LIGHT TECHNOLOGY CO., LTD.). In detail, 5 mg photocatalyst was added in Pyrex top-irradiation photo-reactor with 12 mL aqueous solution containing 3 mL triethanolamine (TEOA). And then, the photo-reactor was connected to a closed gas-circulation for 30 min vacuumizing pretreatment to ensure the reactor was in an anaerobic condition before the photocatalytic experiment. Afterwards, a 300 W Xe lamp was used as the light source with a AM1.5 (100 mW cm^{-2}) for irradiation. During the reaction process, the temperature was controlled at 4 °C by cooling circulating system. The amount of hydrogen gas produced was detected by gas chromatography (BEIJING CHINA EDUCATION AU-LIGHT TECHNOLOGY CO., LTD.) with a TCD detector. The photocatalytic stability was performed in the same experimental factors.

1.10 Photoelectrochemical measurements

The photocurrent measurements, electrochemical impedance spectroscopy (EIS) and Mott-Schottky analysis were performed with an electrochemical workstation (Metrohm Autolab, PGSTAT 302 N) in a standard three-electrode system including a working electrode, a Pt counter electrode, and a Ag/AgCl (saturating KCl) reference electrode. The working electrodes were prepared by the following procedure: the mashed sample (10 mg) was dispersed into 1 mL ethyl alcohol containing 0.5% Nafion to form a slurry. Then, the slurry solution was coated onto a fluorine-doped tin oxide (FTO) glass substrate (1 cm×1 cm) and dried at 70 °C overnight. The 0.2 M Na_2SO_4 was used as the electrolyte solution in all of the electrochemical experiments. The electrochemical impedance spectroscopy (EIS) measurements were carried out with the frequency ranging from 10^{-1} to 10^5 Hz. The Mott-Schottky (MS) plots were obtained under a reverse bias from −1 to 1 V at 500, 1000, and 1500 Hz. Furthermore, amperometric I-t curves were recorded at an applied voltage of 0.6 V with the light on or off to explore the photocurrent response of the samples using 300 W Xe lamp equipped with a 400 nm cutoff filter.

1.11 Comosol heat transfer simulation

In order to comprehend the theoretical implications of the excellent solar-driven thermal sustaining effect on the interfacial photothermal layer of $ZnIn_2S_4/Ti_3C_2/MoS_2$ SNFAs solar-thermal device, and supreme heat management of super hydrophilic two-dimensional cellulose fiber, the heat transfer module (HTM) was simulated using advance COMSOL Multiphysics Simulations.[4] Using the following equation, we evaluated the effective thermal management in steady-state thermal transfer simulations of a three-dimensional macroporous evaporative structure aerogel based on the MXene semiconductor heterojunction structure:

$Q = (\rho C_p)_{\mathrm{eff}} + \rho C_p u \cdot \nabla T + \nabla \cdot q$..........................(1)

$q = -k_{eff} \nabla T$..(2)

$(\rho C_p)_{eff} = \theta_p \rho_p C_{p,p} + (1-\theta_p) \rho C_p$.........................(3)

$k_{eff} = \theta_p k_p + (1-\theta_p) k$.......................................(4)

In the above equations, Q (W m^{-3}) denotes the heat flux, $(\rho C_p)_{\mathrm{eff}}$ provides the effective volume heat capacity under constant pressure, ρ represents the fluid density (1000 kg m^{-3}), and C_p is the fluid heat capacity (4200 J kg^{-1} K^{-1}). The Darcy velocity (u) shows the volume of fluid flow rate per unit cross-sectional area (m s^{-1}), and the fluid velocity inside open pores of natural silk nano-fifibrils porous structure was considered as

$u_L = u/\theta_p$, here θ_p represents the open porous assembly of $ZnIn_2S_4/Ti_3C_2/MoS_2$ SNFAs evaporator. ∇T is the temperature variation (Km^{-1}), and q shows the heat flux vector ($W\ m^{-2}$).

S2. Photothermal Conversion Efficiency

The photothermal conversion efficiency (ŋ) of the TM-ZIS@NSAs aerogels-based solar thermal evaporator was obtained by the following formulation.[4-8]

$$\eta_{evap} = \frac{\dot{m}_v\, h_{LV}}{q_i} \ldots\ldots\ldots\ldots\ldots\ldots\ldots\ldots\ldots\ldots(1)$$

$$h_{LV} = ʎ + C\ \Delta T \ldots\ldots\ldots\ldots\ldots\ldots\ldots\ldots\ldots\ldots(2)$$

$$ʎ = 1.91846 \times 10^6 \times \left(\frac{Tv + 273}{Tv + 239.09}\right)^2 \ldots\ldots\ldots\ldots\ldots\ldots(3)$$

Where $\dot{m}_v$ shows an evaporation rate ($\dot{m}_v$(Ti_3C_2/MoS_2-$ZnIn_2S_4$@NSAs) =2.578 kg m^{-2} h^{-1}) under solar irradiance excluding the evaporation rate of pure water (mass flux), h_{LV} represents the total enthalpy of liquid to vapor phase change including sensible heat and phase enthalpy change, q_i is the incident solar energy (1 kW m^{-2}). The ʎ belongs to the latent heat of phase change which Related to the temperature of the vapor generation by the material (Tv). However, C is the specific heat capacity of water (4.2 kJ kg^{-1} K^{-1}) while △T represents the difference between the temperature of the vapor generated by the material and the ambient temperature. The humidity was kept at 45 % approximately while the environment temperature was 18.01 ± 1 °C during solar-driven experiments. According to these equations (1-3), TM-ZIS@NSAs can generate vapor at 44.3 °C with the corresponding photothermal conversion efficiency (93.496%) excluding optical and thermal losses.

S2.1 Light-absorbing loss

Since the entire reaction test was performed under light and the heat from the ambient environment around the device enhances the evaporation of water, the integral heat loss (5.05%) was examined and the exact evaporation rate of the TM-ZIS@NSAs was deduced. In addition, there are differences in the solar absorption characteristics of different evaporators, and the efficiency of solar absorption is unable to reach 100% which inevitably loss of light absorption in the experiment. For instance, the UV spectrum of TM-ZIS@NSAs revealed an increase in solar absorption (94.95%) by removing optical losses (reflection and transmission). Therefore, the absorbed energy of the evaporator is approached to 949.5 W m^{-2}.

S2.2 Thermal-conversion losses

According to the thermal transport theory, the thermodynamic equilibrium was verified by the stable surface temperature under the solar water evaporation test to analyze the energy balance relationship existing in solar energy input and energy loss, which includes heat conduction, heat convection, and heat radiative. The main pathway of heat loss from the absorber under irradiation includes three portions: conductive heat loss to bulk water ($Q_{Conduction}$), convective ($Q_{Convection}$) and radiative ($Q_{Radiation}$) heat loss to the surroundings.

S2.2.1 Conduction heat loss

Heat transfer losses are motivated by the thermal gradient between objects. When heat flows through a liquid medium from a high temperature source to a low temperature body it leads to heat transfer. The bulk water conduction heat loss ($Q_{Conduction}$) can be computed by the following equation.[9]

$$Q_{Conduction} = Ak\frac{(T_1 - T_2)}{\Delta l} \quad \text{...(4)}$$

Where A is the cross-sectional area of TM-ZIS@NSAs (6×1.5 cm^2), k denotes the thermal conductivity of bulk water (0.599 W m^{-1} K^{-1}). The two embedded thermocouples were applied to monitor the water temperature, and the distance between the thermocouples (Δl) is 5 mm. The average temperature at Point 1(Material upper surface temperature) over one hour is about 28.199 °C. The average temperature at Point 2(Material lower surface temperature) over one hour is about 28.813 °C. Consequently, the $Q_{Conduction}$ is estimated as 6.62 W m^{-2}, corresponding to 0.662%.

S2.2.2 Convective heat loss

The heat dissipates into the environment during evaporation in the form the convective heat loss ($Q_{Convection}$) to the environment, we can use:[10]

$Q_{convection} = h\,(T_s - T_v)$……………………………………………(5)

In this case h designates the convective heat transfer coefficient (presumed to be 10 W m-2 K-1) , which presents the surface temperature of the solar evaporator (44.33°C). Since the surface is enclosed by hot steam, the surrounding temperature can take the steam temperature (41.5°C). Consequently, the $Q_{Convection}$ is estimated as 28.3 W m^{-2}, corresponding to 2.83%.

S2.2.3 Radiative heat loss

Thermal radiation is the electromagnetic radiation emitted by all objects. In this process, there is no need to transfer the medium, and also wu learn to exchange mass. Therefore, the emission and absorption of radiation from all objects depends primarily on the temperature and emissivity of the object relative to its surroundings, and the radiation is proportional to the fourth power of the absolute temperature.The radiative heat loss ($Q_{Radiation}$) to surroundings can be calculated as:[11]

$Q_{Radiation} = \varepsilon\,\sigma\left(T_s^4 - T_\infty^4\right)$…………………………………………(6)

Where ε denotes the emission of the absorber (assumed to be 0.93), σ is the Stefan-Boltzmann constant (5.6703×10^{-8} W m^{-2} K^{-4}), $T_\infty$is the temperature of the adjacent environment. Since the heat is radiated from the interfacial surface towards the surrounding, the surrounding temperature is calculated by $T_\infty = T_a$ (ambient temperature of 18 °C) and the corresponding radiative heat loss is calculated to be 23.32 W m-2, corresponding to 2.332%.

S3. Results

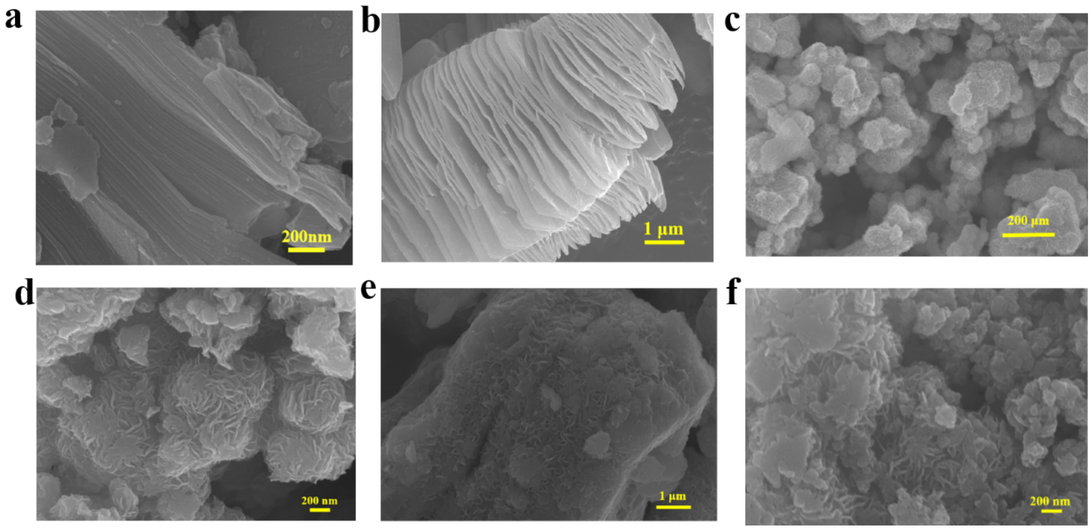

Figure S1. SEM images of (a) Ti_3AlC_2, (b) Ti_3C_2 (MXene), (c) $ZnIn_2S_4$, (d) MoS_2, (e) Ti_3C_2-$ZnIn_2S_4$, and (f) MoS_2-$ZnIn_2S_4$ composite.

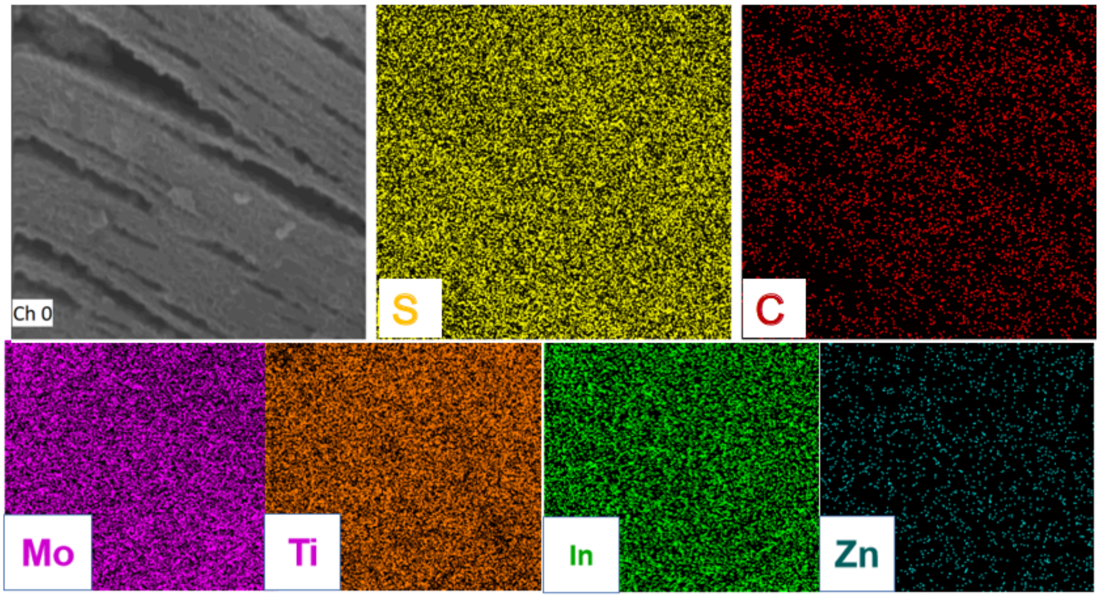

Figure S2. SEM image and corresponding elemental mapping images of Mo, Ti, In, Zn, S elements of Ti_3C_2/MoS_2-$ZnIn_2S_4$.

Figure S3. (a) XRD pattern of Ti_3AlC_2 and Ti_3C_2 (b)Raman pattern of Ti_3C_2

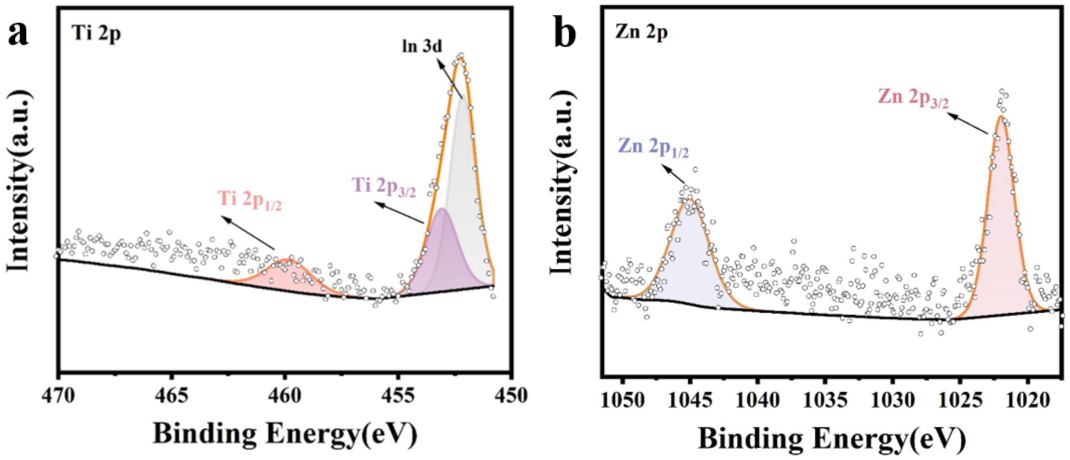

Figure S4. High-resolution XPS spectra for (a)Ti 2p and (b) Zn 2p of $ZnIn_2S_4/Ti_3C_2/MoS_2$ composite.

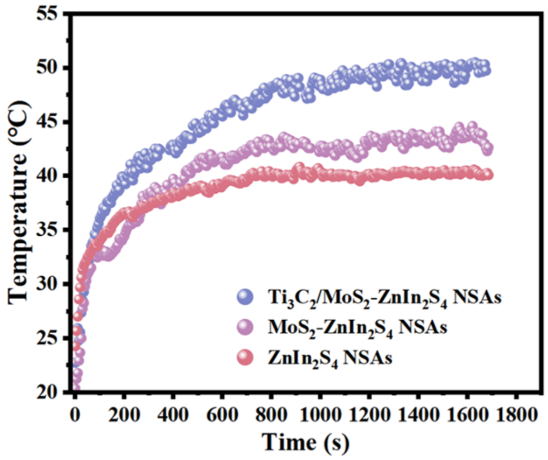

Figure S5. The time-dependent inside temperature of the samples.

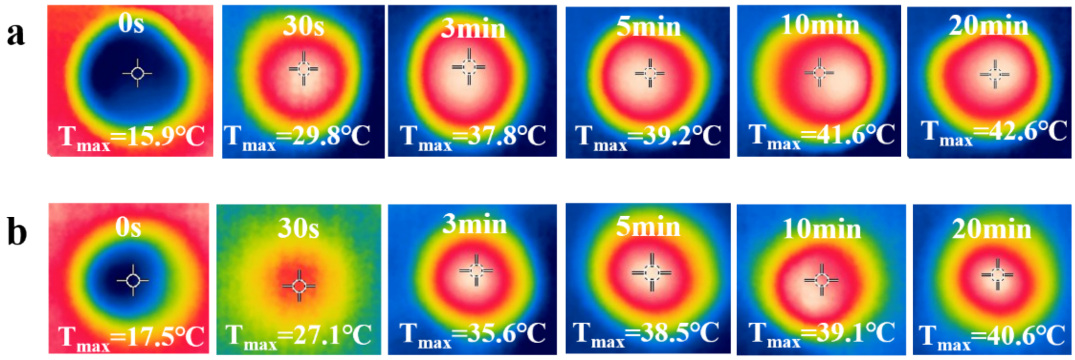

Figure S6. The time-dependent surface temperature of (a) MoS_2-$ZnIn_2S_4$ and (b)$ZnIn_2S_4$.

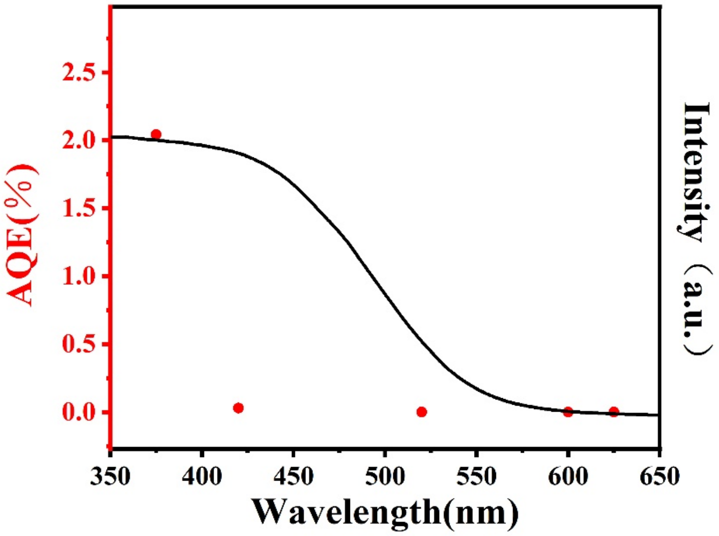

Figure S7. The wavelength-dependent AQE of Ti_3C_2/MoS_2-$ZnIn_2S_4$

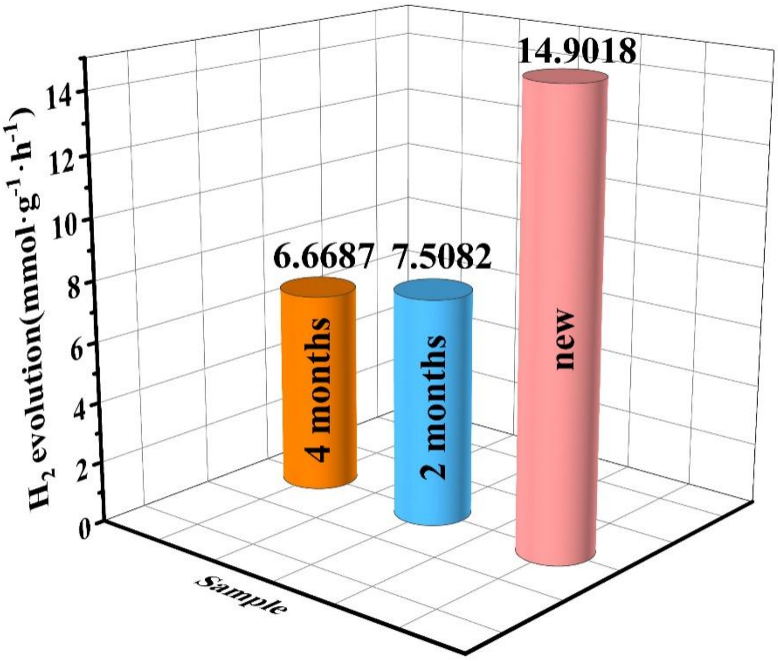

Figure S8. The photocatalytic H_2-evolution rate of Ti_3C_2/MoS_2-$ZnIn_2S_4$ samples set aside for different periods of time（temperature controlled at 0°C）

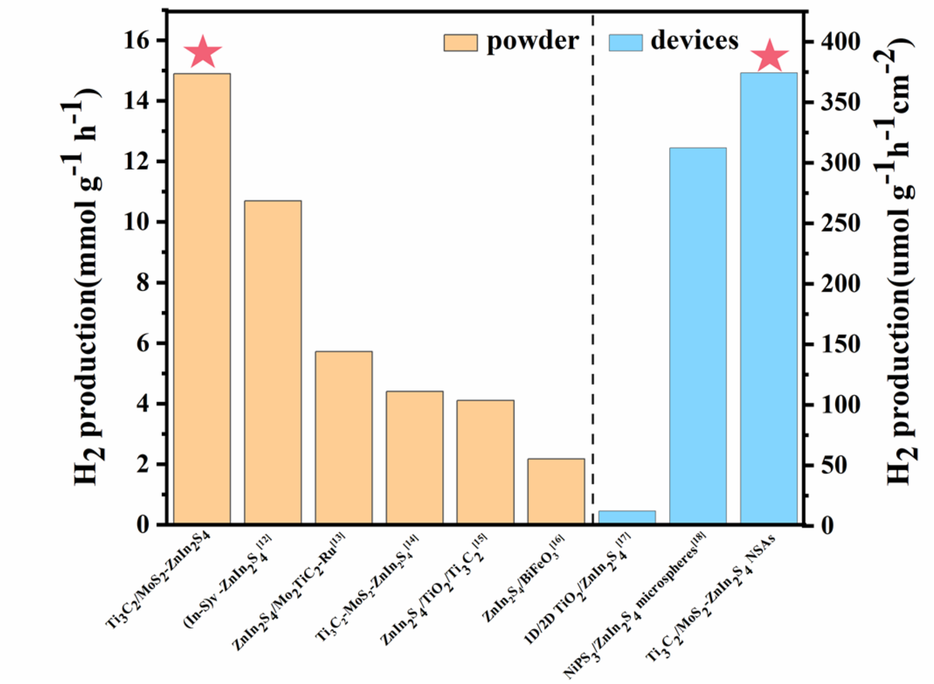

Figure S9. The hydrogen production rate of Ti_3C_2/MoS_2-$ZnIn_2S_4$ powder (at 0 ℃) and NSAs compared to other reported materials.

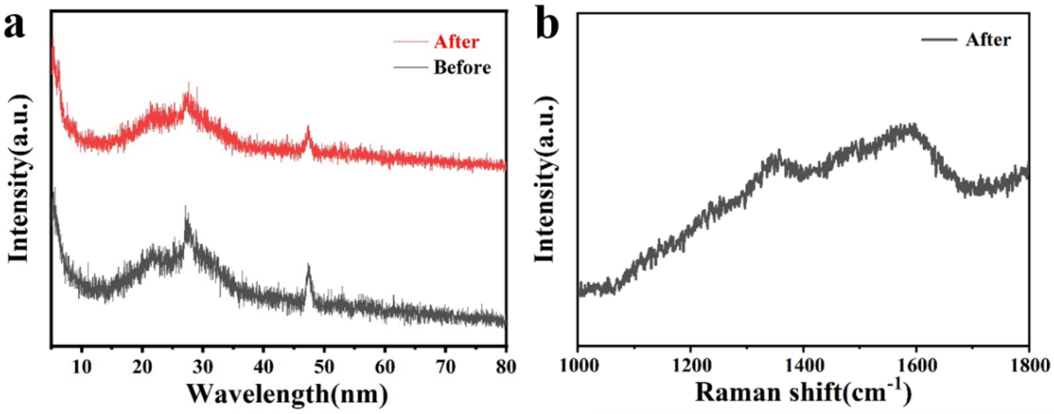

Figure S10. (a) XRD pattern of Ti_3C_2/MoS_2-$ZnIn_2S_4$ before and after photocatalytic water splitting test and (b) Raman pattern of Ti_3C_2/MoS_2-$ZnIn_2S_4$ after photocatalytic water splitting test

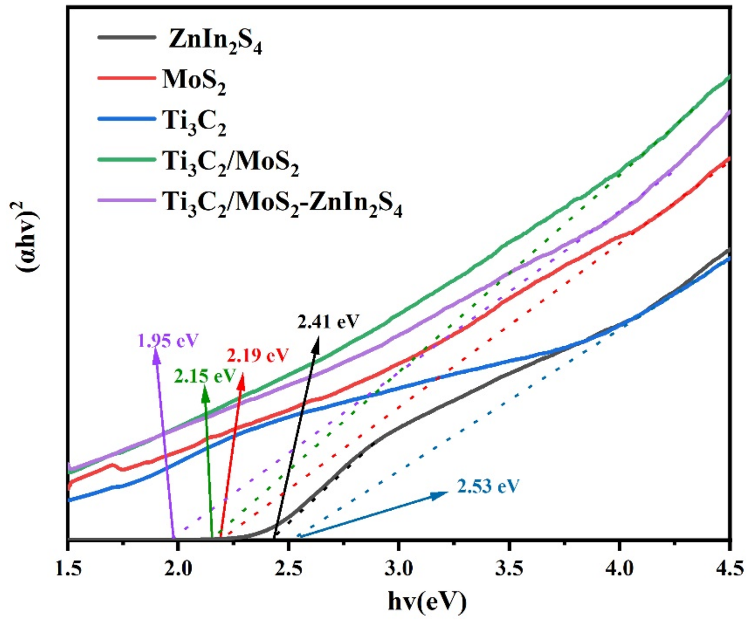

Figure S11. Plot of transformed Tauc plot versus photon energy based on the UV-vis spectra for the various samples: $ZnIn_2S_4$, MoS_2, Ti_3C_2, Ti_3C_2-$ZnIn_2S_4$ and Ti_3C_2/MoS_2-$ZnIn_2S_4$.

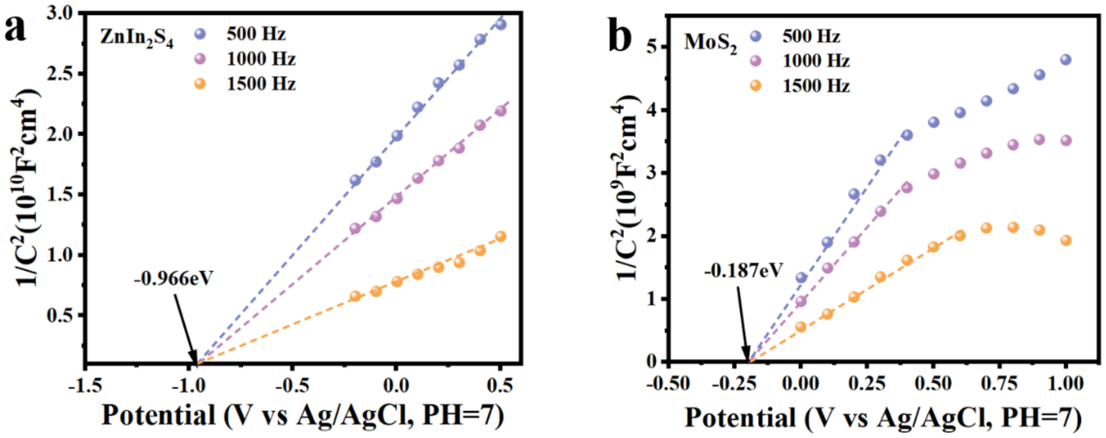

Figure S12. the Mott-Schottky plot of (a) $ZnIn_2S_4$ and (b) MoS_2.

The energy band structures of $ZnIn_2S_4$ and MoS_2 were investigated for further study of the transfer pathways of photogenerated carriers in the photocatalytic process. Mot-Schottky (M-S) plots of $ZnIn_2S_4$ and MoS_2 were collected at AC frequencies of 500, 1000 and 1500 Hz, and the positive slopes in the plots indicate the n-type semiconductor behavior of $ZnIn_2S_4$ and MoS_2. Furthermore, according to previous literature, the conduction band (ECB) of n-type semiconductors is more negative than its Efb by about 0.1 V. Therefore, the flat band potentials of $ZnIn_2S_4$ and MoS_2 are -0.966 eV and -0.187 eV for Ag/AgCl, respectively (-0.866 eV and -

0.087 eV for NHE, normal hydrogen electrode). Based on the band gaps of 2.41 eV and 2.09 eV for $ZnIn_2S_4$ and MoS_2, the VB of $ZnIn_2S_4$ and CB of MoS_2 are 1.544 V and 2.003 eV compared to NHE.

Figure S13. (a) the photo of the top cover of the outdoor experimental setup, (b) vapor condensed in the top cover, and (c) H_2 bubbles in the volumetric cylinder.

	t1	I1	t2	I2
$ZnIn_2S_4$	0.60082	90.94%	8.50971	9.06%
MoS_2-$ZnIn_2S_4$	0.47406	85.48%	3.36921	14.52%
Ti_3C_2-$ZnIn_2S_4$	0.54303	70.44%	2.62802	29.56%
Ti_3C_2/MoS_2-$ZnIn_2S_4$	0.46429	91.54%	3.38992	8.46%

Table S1. The fitting parameters of the time-resolved PL (TRPL) were fitted using the biexponential kinetics function.

Supplementary Reference

1. A. Feng, Y. Yu, Y. Wang, F. Jiang, Y. Yu, L. Mi and L. Song, *Mater. Des.*, 2017, **114**, 161-166.
2. Z. Guo, Z. Chen, Z. Shi, J. Qian, J. Li, T. Mei, J. Wang, X. Wang and P. Shen, *Sol. Energy Mater. Sol. Cells*, 2020, **204**, 110227.

3. Q. Wang, S. Yan, G. Han, X. Li, R. You, Q. Zhang, M. Li and D. L. Kaplan, *Compos. Sci. Technol.*, 2020, **187**, 107950.
4. M. S. Irshad, N. Arshad, X. Wang, H. R. Li, M. Q. Javed, Y. Xu, L. A. Alshahrani, T. Mei and J. Li, *Sol. RRL*, 2021, **5**, 2100427.
5. M. S. Irshad, X. Wang, M. S. Abbasi, N. Arshad, Z. Chen, Z. Guo, L. Yu, J. W. Qian, J. You and T. Mei, *ACS Sustainable Chem. Eng.*, 2021, **9**, 3887-3900.
6. C. Song, M. S. Irshad, Y. Jin, J. Hu and W. Liu, *Desalination*, 2022, **544**, 116125.
7. M. Sultan Irshad, X. Wang, N. Arshad, M. Q. Javed, T. Shamim, Z. Guo, H.-R. Li, J. Wang and T. Mei, *Environ. Sci.: Nano*, 2022, **9**.
8. M. S. Irshad, Y. Hao, N. Arshad, M. Alomar, L. Lin, X. Li, S. Wageh, O. A. Al-Hartomy, A. G. Al-Sehemi, V.-D. Dao, H. Wang, X. Wang and H. Zhang, *Chem. Eng. J.*, 2023, **458**, 141431.
9. Z. Deng, P.-F. Liu, J. Zhou, L. Miao, Y. Peng, H. Su, P. Wang, X. Wang, W. Cao, F. Jiang, L. Sun and S. Tanemura, *Sol. RRL*, 2018, **2**, 1800073.
10. P. Zhang, Q. Liao, H. Yao, Y. Huang, H. Cheng and L. Qu, *Energy Storage Mater.*, 2019, **18**, 429-446.
11. L. Cui, P. Zhang, Y. Xiao, Y. Liang, H. Liang, Z. Cheng and L. Qu, *Adv. Mater.*, 2018, **30**, 1706805.
12. P. Zhang, J. Lin, J. Zhao, C. Lu, L. Huang, Z. Lin, D. Bu and S. Huang, *Renewable Energy*, 2024, **237**, 121741.
13. Q. Xi, J. Liu, F. Xie, A. Jian, Z. Sun, A. Zhou, X. Jian, X. Zhang, Y. Wang, H. Li, X. Gao, J. Ren, C. Fan, J. Wang and R. Li, *Applied Catalysis B: Environment and Energy*, 2024, **355**, 124184.
14. L. Ma, L. Xu, Y. Ding, C. Lin, Y. Yang and X. Ai, *Int. J. Hydrogen Energy*, 2024, **82**, 713-723.
15. D.-E. Lee, M. V. Jyothirmai, S. Moru, W.-K. Jo and S. Tonda, *J. Water Process Eng.*, 2024, **67**, 106202.
16. P. Su, D. Zhang, X. Yao, T. Liang, N. Yang, D. Zhang, X. Pu, J. Liu, P. Cai and Z. Li, *J. Colloid Interface Sci.*, 2024, **662**, 276-288.
17. Y. Liang, Y. Xiao, X. Lv, Y. Sui, M. Guo, L. Bai, H. Yang, D. Wei, W. Wang and L. Yang, *Mater. Sci. Semicond. Process.*, 2024, **181**, 108632.
18. J. Hu, J. Li, X. Liu, W. Xiao, H. Yu, H. Abdelsalam, C. Liu, Z. Zou and Q. Zhang, *J. Colloid Interface Sci.*, 2025, **680**, 506-515.